molecules

MDPI

Article

Enhanced Electrocatalytic Performance of P-Doped MoS_2/rGO Composites for Hydrogen Evolution Reactions

Wenjun Zhu [1,2,3,*], Bofeng Zhang [1], Yao Yang [2], Minghai Zhao [1], Yuwen Fang [1], Yang Cui [3] and Jian Tian [4,*]

[1] School of Mechanical and Electrical Engineering, Jingdezhen Ceramic University, Jingdezhen 333403, China
[2] Jingdezhen Mingxing Aerospace Forging Co., Ltd., Jingdezhen 333403, China
[3] Richangsheng Architectural New Materials Design Research lnstitute Co., Ltd., Hangzhou 310000, China
[4] School of Materials Science and Engineering, College of Chemical and Biological Engineering, Shandong University of Science and Technology, Qingdao 266590, China
* Correspondence: zhuwj@zju.edu.cn or zwj2730038@126.com (W.Z.); jiantian@sdust.edu.cn (J.T.)

Abstract: This study is based on the strategies of composite and element doping. Herein, P-MoS_2/rGO materials were synthesized using a solvent-assisted hydrothermal method. The MoS_2 nanosheets were uniformly and vertically grown on rGO; meanwhile, the optimized structure of MoS_2 was achieved by P doping, resulting in improved catalytic performance and structural stability. Under alkaline conditions, the P-MoS_2/rGO catalyst exhibits good electrocatalytic activity, demonstrating a Tafel slope of 70.7 mV dec^{-1} and an overpotential of 172.8 mV at 10 mA/cm^2. Notably, even after 3000 consecutive LSV tests, the curves still show a high degree of overlap, indicating exceptional stability.

Keywords: MoS_2; P-doped; rGO; HER; alkaline condition

check for updates

Academic Editor: César Augusto Correia de Sequeira

Received: 14 January 2025
Revised: 26 February 2025
Accepted: 4 March 2025
Published: 7 March 2025

Citation: Zhu, W.; Zhang, B.; Yang, Y.; Zhao, M.; Fang, Y.; Cui, Y.; Tian, J. Enhanced Electrocatalytic Performance of P-Doped MoS_2/rGO Composites for Hydrogen Evolution Reactions. *Molecules* **2025**, *30*, 1205. https://doi.org/10.3390/molecules30061205

Copyright: © 2025 by the authors. Licensee MDPI, Basel, Switzerland. This article is an open access article distributed under the terms and conditions of the Creative Commons Attribution (CC BY) license (https://creativecommons.org/licenses/by/4.0/).

1. Introduction

As global energy demands surge and concerns over climate change escalate, transitioning from fossil fuels to sustainable energy sources has become critical [1–3]. Hydrogen, known for its clean combustion that generates only water as a byproduct, presents a promising alternative for mitigating greenhouse gas emissions typically associated with conventional energy sources [4–6]. Conventional hydrogen production techniques, including steam reforming and coal gasification, are frequently associated with high carbon emissions and energy consumption. In contrast, the hydrogen evolution reaction (HER) through water electrolysis enables the production of clean hydrogen, positioning it as a key direction in the green energy transition [7,8].

The advancement of efficient catalysts is essential for facilitating hydrogen production through the HER. In acidic HERs, protons (H^+) are readily available in the electrolyte, enabling a direct electron transfer step ($H^+ + e^- \rightarrow H^*$) to form adsorbed hydrogen (H^*). In contrast, in alkaline HER, the reaction requires an additional water dissociation step ($H_2O + e^- \rightarrow H^* + OH^-$) to generate protons before the electron transfer can occur. This extra step makes the alkaline HER significantly slower and more energy-intensive due to the need to break the strong H-O bond in water [9–11]. This fundamental difference underscores the need for advanced catalyst design to overcome the kinetic limitations of HERs in alkaline environments [12]. Conventional precious metal catalysts, like platinum and palladium, demonstrate excellent catalytic performance in electrocatalytic reactions under alkaline conditions; however, they face issues such as high cost and resource scarcity during long-term use. In contrast, molybdenum disulfide (MoS_2) has garnered significant attention due to its excellent catalytic properties, stability in corrosive environments, and

natural abundance [13–15]. The active sites of MoS_2, primarily located at the edges, are crucial for HER efficiency, leading researchers to explore various strategies to maximize their availability. Recent research has primarily focused on modifying the morphology of MoS_2 to increase its surface area and the density of active sites [16–18]. Despite some progress, MoS_2 tends to aggregate during the reaction process and has poor conductivity, which results in suboptimal catalytic performance and stability. The composite design with high-conductivity materials, such as graphene or reduced graphene oxide, effectively enhances the material's conductivity, promoting electron transfer and improving electrocatalytic performance. In addition, element doping is an effective method to significantly improve HER activity, as doping not only enhances the morphology of MoS_2 but also activates its inert basal plane, resulting in the increased active sites and thereby improved HER performance. For instance, by introducing phosphorus (P) atoms into the MoS_2 lattice, the number of active sites can be significantly increased, and the electrical conductivity can be improved, thereby enhancing its performance in the electrocatalytic HER. Typically, phosphorus doping needs to be achieved through complex chemical vapor deposition (CVD) or high-temperature annealing processes. These methods often require precise control of the reaction conditions and a relatively long processing time, which increases the complexity and cost of preparation [19–21].

Therefore, to improve catalytic activity and structural stability, P-MoS_2/rGO composites were designed and fabricated using a straightforward one-step hydrothermal approach. The morphology and microstructure of MoS_2 were optimized by P doping, and the P-doped MoS_2 (with enlarged interlayer spacing and well dispersion, etc.) uniformly grew on the surface of rGO, improving the conductivity and the number of active sites as well as reducing the aggregation. Consequently, the P-MoS_2/rGO composite demonstrates excellent HER performance in an alkaline (1.0 M KOH) solution (Figure 1).

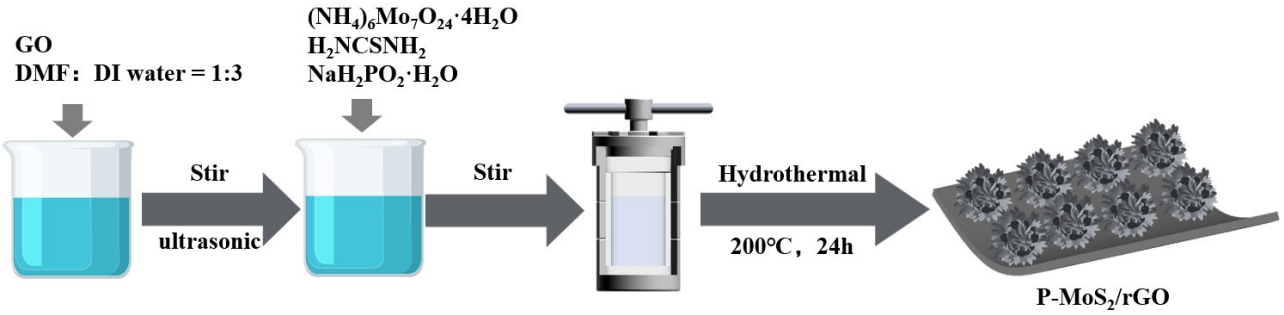


Figure 1. The synthetic process of P-MoS_2/rGO composite.

2. Results and Discussion

As shown in Figure 2a, XRD analysis reveals that in the MoS_2/rGO composite, prominent peaks are observed at 9.7° and 57.6°, corresponding to the (002) and (110) planes of 1T-MoS_2, respectively. Furthermore, a peak at 32.6° corresponds to the (100) plane of 2H-MoS_2 (JCPDS 37-1492) [22]. A similar XRD curve is detected from the P-MoS_2/rGO composite, indicating that the introduction of P does not lead to the formation of new phases. Meanwhile, compared with the MoS_2/rGO composite, the (002) peak of the P-MoS_2/rGO composite shifts to a lower angle at 9°, which demonstrates that the enlarged interlayer spacing can be obtained after P doping. According to the Bragg's law ($2d\sin\theta = n\lambda$), the interlayer spacing of the (002) crystal plane is calculated to change from 0.75 nm to 0.83 nm [23]. Notably, the XRD patterns for both samples lack any distinct peaks attributed to GO or rGO, which can be attributed to their low abundance or effective dispersion within the matrix [24]. Moreover, the XPS tests were undertaken, and the results

are shown in Figure 2b–f. In the XPS survey (Figure 2b), elements such as O, Mo, C, S, and P can be detected in both the MoS_2/rGO and P-MoS_2/rGO composites. According to the XPS survey, the Mo:S molar ratios in MoS_2/rGO and P-MoS_2/rGO are approximately 1:2 and 1:1.8, respectively. Compared with MoS_2/rGO, the increased Mo: S molar ratio in the P-MoS_2/rGO composite is attributed to the fact that some S atoms in the MoS_2 lattice are replaced by P [25]. Moreover, the P-doping process may also lead to the generation of local lattice distortions or defects, further reducing the stability of S and resulting in the loss of S [26]. In the high-resolution Mo 3d spectrum of MoS_2/rGO (Figure 2c), peaks corresponding to S 2s (~225.9 eV), Mo^{4+} $3d_{5/2}$ (~228.9 eV), Mo^{4+} $3d_{3/2}$ (~231.9 eV), and Mo^{6+} $3d_{3/2}$ (~235.4 eV) can be observed. It is evident that new peaks corresponding to Mo^{3+} $3d_{5/2}$ (229.7 eV and 233.1 eV) are observed in the Mo spectrum of P-MoS_2/rGO, which can be attributed to the interaction between Mo and the less electronegative doping P atoms [21]. From the S spectrum (Figure 2d), two peaks corresponding to S $2p_{3/2}$ and S $2p_{1/2}$ are detected, which are located at 161.6 and 162.7 eV. In Figure 2e, three main peaks are found in the C 1s spectrum, including C=C/C-C (~284.4 eV), C-O (~285.7 eV), and C=O (~288.7 eV). The C=C/C-C peak comes from the benzene framework in graphene, while the C-O and C=O peaks originate from the oxidation of graphene [27]. Figure 2f shows that the P 2p spectrum peaks at 137.9, 129.4, and 133.0 eV are attributed to PO_4^{3-}, P $2p_{3/2}$ and P $2p_{1/2}$, respectively, indicating the successful incorporation of P into MoS_2/rGO. Based on the above characterization results, the successful preparation of the samples (MoS_2/rGO and P-MoS_2/rGO composite) is confirmed.

As presented in Figure 3a, unevenly distributed flower-like structures self-assembled from nanosheets can be found in the MoS_2/rGO composite. Moreover, as displayed in the high-magnification SEM image (Figure 3b), there is significant aggregation among these nanosheets, and some blocks or granular materials (marked by) can be observed, which hinders the exposure of active sites. Compared with the MoS_2/rGO composite, a similar flower-like structure, which is more evenly distributed and smaller in size (approximately 220 nm in diameter), can be detected from the P-MoS_2/rGO composite (Figure 3c). Furthermore, as shown in Figure 3d, the flower-like structure of MoS_2 is well formed (just like blooming flowers), and a porous structure can be acquired from the crosslinking effect of these nanosheets without interlayer aggregation, blocks, or granular materials, which is beneficial for providing more active sites [28]. Moreover, the different P-doping concentrations have an important effect on the morphology of the P-MoS_2/rGO composites. As shown in Figure S1, significant aggregation among the nanosheets can be detected from P-MoS_2/rGO-1 and P-MoS_2/rGO-5 composites, which hinders the exposure of the active sites. Figure 3e–h present the EDS results, the uniform distribution of elements, especially the P element, and confirm the successful and uniform doping of P.

The microstructural characteristics of the composites were studied by TEM. As observed in the low-magnification TEM images in Figure 4a,b,d,e, MoS_2/rGO exhibits numerous dark regions, whereas the P-MoS_2/rGO shows more bright areas, indicating that the P-MoS_2/rGO possesses a distinct porous structure derived from the co-crosslinking of nanosheets, aligning with the SEM results. As shown in the high-magnification images (Figure 4c,f), distinct lattice fringes with spacings of 0.73 nm and 0.82 nm are observed from both samples, corresponding to the (002) plane of 1T-MoS_2. In accordance with the XRD results, the increased interlayer can be found in the P-MoS_2/rGO composite, which is attributed to the P-doping effect. Furthermore, a comparison of Figure 4c,f shows that the lattice fringes in the P-MoS_2/rGO composite exhibit distortion, indicating that the P doping has an effect on the microstructure (such as local defect, etc.); this in turn effectively improves electron transport and increases the catalytic activity of reaction sites [29].

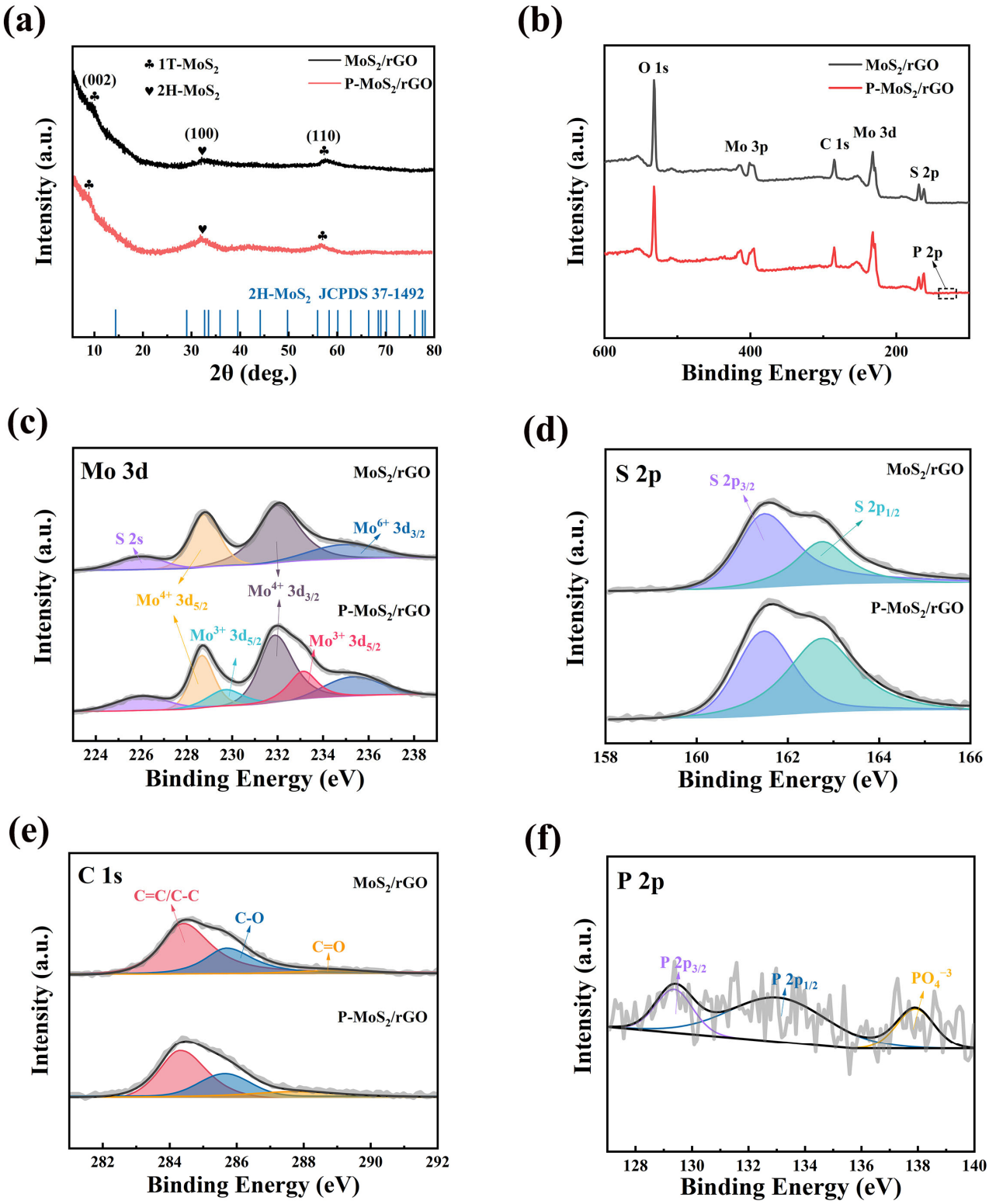


Figure 2. Chemical components of MoS_2/rGO and P-MoS_2/rGO, (**a**) XRD pattern, (**b**) XPS survey spectrum, XPS results of (**c**) Mo 3d, (**d**) S 2p, (**e**) C 1s, and (**f**) P 2p, respectively.

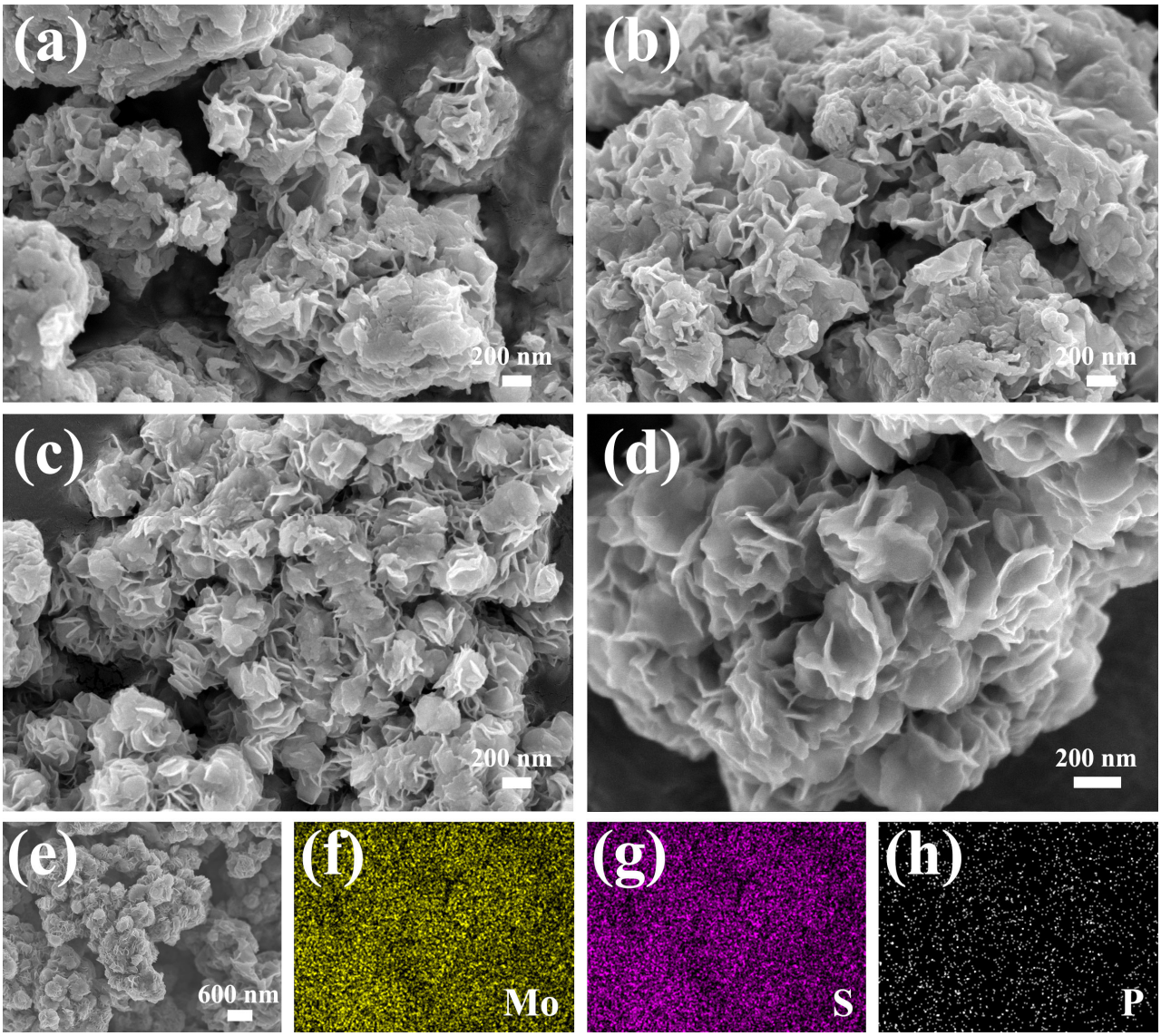


Figure 3. SEM results of the (**a**,**b**) MoS_2/rGO, (**c**,**d**) P-MoS_2/rGO, and (**e**–**h**) corresponding element mapping images of P-MoS_2/rGO.

The catalytic performance of the catalyst for HER was assessed, as shown in Figure 5. The linear sweep voltammetry (LSV) test (with a scan rate of 5 mV s^{-1}) results are shown in Figure 5a with commercial Pt/C electrode for comparison. At 10 mA cm^{-2}, the observed overpotentials of P-MoS_2/rGO, MoS_2/rGO, and Pt/C are 172.8, 228.4, and 44.7 mV, respectively, with corresponding Tafel slopes (Figure 5b) of 70.7, 98.5, and 69.4 mV dec^{-1}, respectively. Compared with the MoS_2/rGO composite, the P-MoS_2/rGO composite displays superior HER performance with a lower overpotential and Tafel slope [30]. Moreover, as shown in Figure S2, the corresponding overpotentials of P-MoS_2/rGO-1 and P-MoS_2/rGO-5 composites are 205.2 mV and 230.5 mV, respectively. It is likely that a higher P concentration leads to excessive aggregation and phase instability, while a lower concentration fails to fully optimize the structure and electronic states, resulting in a decrease in the catalytic performance [31,32]. The electrochemical active surface area (ECSA) has an important effect on the HER performance, which can be evaluated in terms of double-layer capacitance (C_{dl}). As shown in Figure 5c, the C_{dl} values were obtained according to the CV tests conducted at 20–100 mV s^{-1}, and the corresponding values of both samples are 14.7 and 25.8 mF cm^{-2}, respectively. That is to say, the improved

electrochemical active sites can be obtained after P doping, which is attributed to the enlarged interlayer distance and optimized microstructure.

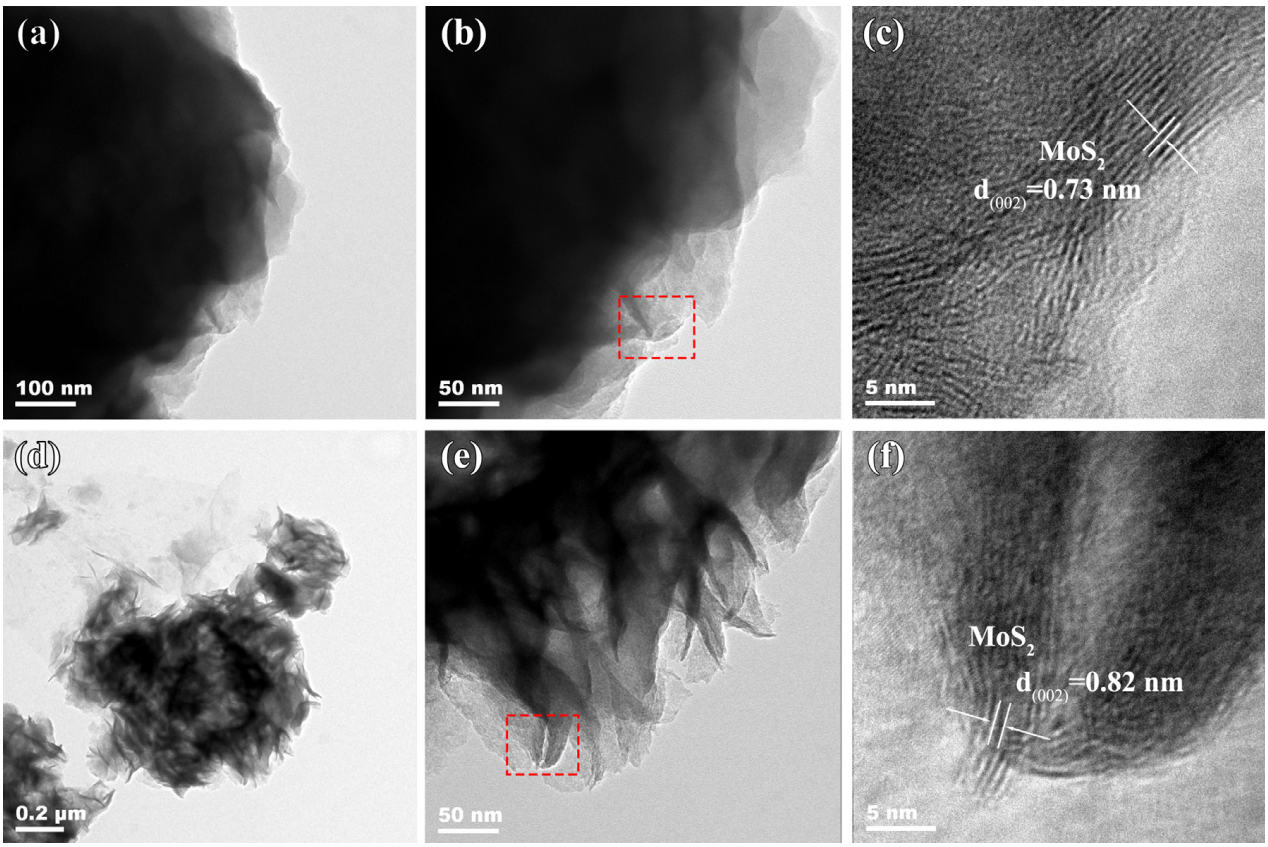


Figure 4. The TEM results of the (**a**–**c**) MoS_2/rGO and (**d**–**f**) P-MoS_2/rGO. (**c**,**f**) are the corresponding enlarged images of the red boxes in (**b**,**e**), respectively.

When evaluating the catalytic performance for HER, stability is a vital consideration. The LSV curves for the P-MoS_2/rGO composite before and after 3000 potential cycles are presented in Figure 5d, which exhibit almost no change in shape, indicating a negligible decay in performance [33]. Moreover, the chrono-potentiometric test was conducted, as shown in Figure 5e. It can be found the potential remains stable over a 24 h period, demonstrating the excellent durability of the P-MoS_2/rGO composite. EIS test was performed to further explain the superior HER performance, with fitting performed using an equivalent circuit model (inset), and the results are presented in Figure 5f. Compared with MoS_2/rGO composite, the semicircle (R_{ct}) with the smaller radius indicates an improved electron and charge transfer properties that can be achieved for the P-MoS_2/rGO composite, and the corresponding R_{ct} values for both products are 22.3 and 59.6 Ω, respectively. Thus, the enhanced HER kinetics can be achieved for the P-MoS_2/rGO composite [34]. Table 1 compares the catalytic performance of existing MoS_2-based composites with our work. It can be observed that the P-MoS_2/rGO composite in this work exhibits comparable catalytic performance, which can be attributed to the following several factors: Firstly, it is derived from the composite with rGO and P doping, resulting in improved conductivity. Furthermore, the optimized structure with enlarged interlayer spacing and well dispersion can be obtained by the P doping effect, providing abundant reaction sites and alleviating the stacking issue of MoS_2. Notably, when the doping level of P in the P-MoS_2/rGO composite material reaches the optimal state, it features a structure with a porous and uniform

flower-like morphology. Thus, improved catalytic performance and structural stability can be achieved by the P-MoS_2/rGO composite.

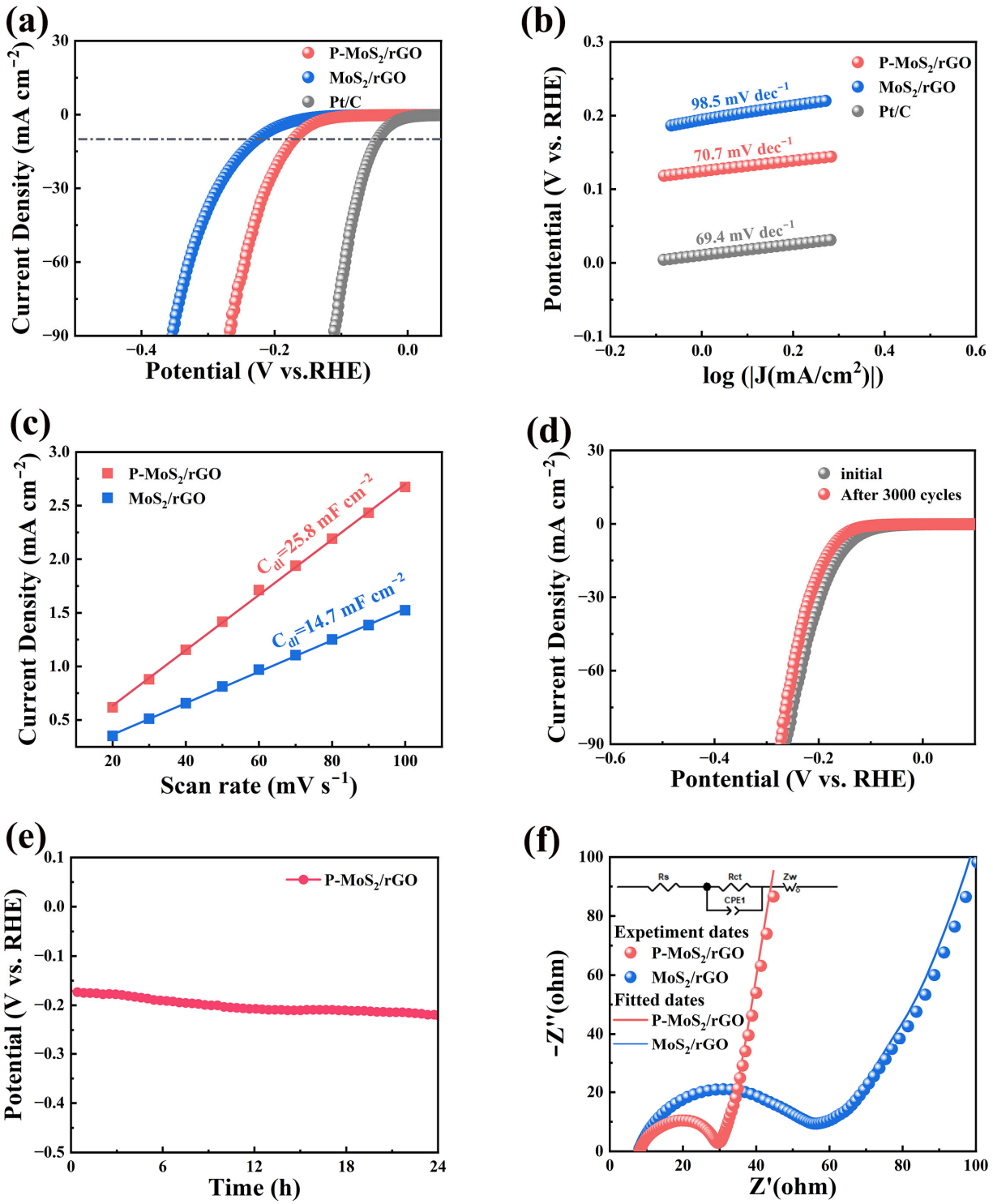


Figure 5. (**a**) Polarization curves, (**b**) Tafel slopes, and (**c**) C_{dl} values. Stability performance of P-MoS_2/rGO material: (**d**) polarization curves and (**e**) time-dependent curves, (**f**) Nyquist plots.

Table 1. Compared with the existing MoS_2-based composites.

Materials	Electrolyte	η_{10} (mV)	Tafel Slope (mV dec^{-1})	Refs
MoS_2/SN-rGO	0.5 M H_2SO_4	650	184	[35]
MoS_2-500	0.5 M H_2SO_4	355	84	[36]
M1S1	0.5 M H_2SO_4	248	84	[37]
rGO-MoS_2	0.5 M H_2SO_4	207	-	[38]
Mn-MoS_2/rGO	0.5 M H_2SO_4	230	76	[39]
500-MoS_2	0.5 M H_2SO_4	180	47	[40]
MoS_2/TiO_2	1 M KOH	700	60	[41]
0.2 GO-MoS_2 NIR	1 M KOH	314	80	[42]
Co_3O_4/MoS_2	1 M KOH	205	128	[43]
MoS_2/G HS	1 M KOH	183	127	[44]
MoS_2/Ni_3S_2	1 M KOH	190	65.6	[45]
P-MoS_2/rGO	1 M KOH	172.8	70.7	This work

3. Experimental Section

3.1. Materials Synthesis

Reagents of analytical grade were used in this study without the need for further purification. As illustrated in Figure 1, 0.05 g of graphene oxide (GO, Suzhou Carbon Rich Graphene Technology Co., Ltd, Suzhou, China) was initially combined with 12 mL of deionized water and 4 mL of dimethylformamide (DMF, Shanghai Aladdin Biochemical Technology Co., Ltd, Shanghai, China), followed by stirring and ultrasonication for 1 h to achieve a uniform dispersion. Next, 0.4 g of thiourea (H_2NCSNH_2, Tianjin Fengchuan Chemical Technology Co., Ltd., Tianjin, China), 0.2 g of ammonium heptamolybdate tetrahydrate ($(NH_4)_6Mo_7O_{24}\cdot 4H_2O$, Tianjin Damo Chemical Reagent Factory, Tianjin, China) and 0.03 g of Sodium hypophosphite monohydrate ($NaH_2PO_2\cdot H_2O$, Xilong Science Co., Ltd, Shantou, China) were added to the solution. A hydrothermal synthesis was then conducted at 180 °C for 24 h. The resulting product was subsequently ultrasonically washed to eliminate any organic contaminants and dried (60 °C for 18 h), obtaining the P-MoS_2/rGO composites. In order to investigate the effect of different P-doping concentrations, the samples with the addition amounts of $(NH_4)_6Mo_7O_{24}\cdot 4H_2O$ being 0.01 g and 0.05 g were prepared for comparison, which were labeled as P-MoS_2/rGO-1 and P-MoS_2/rGO-5, respectively. For comparative purposes, MoS_2/rGO was synthesized under the same conditions, omitting the addition of $NaH_2PO_2\cdot H_2O$.

3.2. Material Characterization

A powder X-Ray diffractometer (XRD; D8 Advance, Bruker AXS GmbH, Bellerica, MA, USA) equipped with Cu Kα radiation (λ = 0.15418 nm) was used to investigate the phase composition of the synthesized materials. The surface chemical composition and electronic states were studied using X-Ray photoelectron spectroscopy (XPS) on a Thermo Scientific K-Mura Alpha+ instrument (Thermo Scientific, Shanghai, China). To investigate the morphological features and microstructural properties, scanning electron microscopy (SEM; SU-8020, HITACHII, Beijing, China) and transmission electron microscopy (TEM; JEM-2100, JEOL, Beijing, China) were employed.

3.3. Electrochemical Measurements

A three-electrode device with a 1.0 M KOH electrolyte was used for the electrochemical measurements in which the Hg/HgO, glassy carbon electrode (4 mm in diameter) and graphite rod were used as the reference, working, and counter electrodes, respectively. All the results of cyclic voltammetry (CV), linear sweep voltammetry (LSV), current-voltage

(I–V), and electrochemical impedance spectroscopy (EIS, 0.1 Hz–100 kHz) were recorded on an electrochemical workstation (CHI 660E, Chenhua, Shanghai, China). In the preparation process of the working electrode, 5 mg of the synthesized catalyst sample was dispersed in 1 mL mixture of 5% Nafion and anhydrous ethanol (with a volume ratio of 1:49). Following 2 h of ultrasonication, 5.0 μL of the catalyst suspension was evenly spread on the surface of the working electrodes and dried at room temperature for subsequent test. During the electrochemical measurements, the potentials were calibrated with reversible hydrogen electrode (RHE) according to the equation: $E_{RHE} = E_{Hg/HgO} + 0.0592 \times pH + 0.098$.

4. Conclusions

In summary, this study presents a simple solvent-assisted hydrothermal method to synthesize P-MoS_2/rGO materials. Based on the P-doping effect, the morphology and structure of MoS_2 nanosheets were regulated, and the optimized MoS_2 nanosheets (with enlarged interlayer spacing and well dispersion, etc.) were uniformly and vertically grown on rGO. Owing to the unique structure, improved conductivity, abundant reaction sites, and excellent structural stability can be achieved. As a result, the P-MoS_2/rGO composite delivers superior HER electrocatalytic performance and cyclic stability, with an overpotential of 172.8 mV and a Tafel slope of 70.7 mV dec^{-1} at 10 mA/cm^2. This work offers a simpler and more scalable synthesis route, while achieving comparable catalytic performance under alkaline conditions. These findings highlight the potential of P-MoS_2/rGO composites as efficient and durable electrocatalysts for hydrogen production.

Supplementary Materials: The following supporting information can be downloaded at: https://www.mdpi.com/article/10.3390/molecules30061205/s1, Figure S1: SEM results of (a) P-MoS_2/rGO-1 and (b) P-MoS_2/rGO-5; Figure S2: Polarization curves.

Author Contributions: Conceptualization, W.Z.; methodology, W.Z., B.Z. and Y.Y.; software, Y.Y., B.Z. and M.Z.; validation, W.Z., B.Z. and Y.F.; formal analysis, Y.Y., B.Z., Y.F. and Y.C.; investigation, B.Z. and M.Z.; resources, W.Z., J.T. and Y.C.; data curation, B.Z. and Y.Y.; writing—original draft preparation, B.Z. and W.Z.; writing—review and editing, W.Z.; visualization, W.Z. and B.Z.; supervision, W.Z. and J.T.; project administration, W.Z. and J.T.; funding acquisition, W.Z. All authors have read and agreed to the published version of the manuscript.

Funding: This research was funded by [the Natural Science Foundation of Jiangxi Province, China] [No. 20232BAB204020], [the National Natural Science Foundation of China] [No. 51802131, 51872173], and [Jiangxi Provincial Postgraduate Innovation Fund] [JYC202317].

Institutional Review Board Statement: Not applicable.

Informed Consent Statement: Not applicable.

Data Availability Statement: Data are contained within the article and Supplementary Materials.

Conflicts of Interest: Authors Wenjun Zhu and Yao Yang were employed by the company Jingdezhen Mingxing Aerospace Forging Co., Ltd., Jingdezhen, China. Authors Wenjun Zhu and Yang Cui were employed by the company Richangsheng Architectural New Materials Design Research lnstitute Co., Ltd., Hangzhou, China. The remaining authors declare that the research was conducted in the absence of any commercial or financial relationships that could be construed as a potential conflict of interest.

References

1. Zhou, Q.; Wang, Z.; Yuan, H.; Wang, J.; Hu, H. Rapid hydrogen adsorption-desorption at sulfur sites via an interstitial carbon strategy for efficient HER on MoS_2. *Appl. Catal. B Environ.* **2023**, *332*, 122750. [CrossRef]
2. Guo, D.; Wan, Z.; Fang, G.; Zhu, M.; Xi, B. A tandem interfaced (Ni_3S_2-MoS_2)@TiO_2 composite fabricated by atomic layer deposition as efficient HER electrocatalyst. *Small* **2022**, *18*, 2201896. [CrossRef] [PubMed]

3. Xiao, J.; Wang, B.; Shu, Q. MXene Anchored with Platinum Cobalt Alloy as an Efficient and Stable Electrocatalyst for Hydrogen Evolution. *Molecules* **2024**, *29*, 5793. [CrossRef] [PubMed]
4. Rhuy, D.; Lee, Y.; Kim, J.Y.; Kim, C.; Kwon, Y.; Preston, D.J.; Kim, I.S.; Odom, T.W.; Kang, K.; Lee, D. Ultraefficient electrocatalytic hydrogen evolution from strain-engineered, multilayer MoS_2. *Nano Lett.* **2022**, *22*, 5742–5750. [CrossRef]
5. Liu, X.; Li, Z.; Jiang, H.; Wang, X.; Xia, P.; Duan, Z.; Ren, Y.; Xiang, H.; Li, H.; Zeng, J. Enhanced HER Efficiency of Monolayer MoS2 via S Vacancies and Nano-Cones Array Induced Strain Engineering. *Small* **2024**, *20*, 2307293. [CrossRef]
6. Li, T.; Chen, J.; Song, Z.; Zhong, S.; Feng, W. FeNi-Based Aerogels Containing $FeNi_3$ Nanoclusters Embedded with a Crystalline–Amorphous Heterojunction as High-Efficiency Oxygen Evolution Catalysts. *Molecules* **2024**, *29*, 5429. [CrossRef]
7. Venkateshwaran, S.; Devi, P.; Murugan, P.; Senthil Kumar, S.M. Simple immersion in polar solvents induces targeted 1T phase conversion of MoS_2 for HER: A greener approach. *ACS Appl. Energy Mater.* **2023**, *7*, 1037–1050. [CrossRef]
8. Fu, K.; Yuan, D.; Yu, T.; Lei, C.; Kou, Z.; Huang, B.; Lyu, S.; Zhang, F.; Wan, T. Recent Advances on Two-Dimensional Nanomaterials Supported Single-Atom for Hydrogen Evolution Electrocatalysts. *Molecules* **2024**, *29*, 4304. [CrossRef]
9. Xu, H.G.; Zhang, X.Y.; Ding, Y.; Fu, H.Q.; Wang, R.; Mao, F.; Liu, P.F.; Yang, H.G. Rational design of hydrogen evolution reaction electrocatalysts for commercial alkaline water electrolysis. *Small Struct.* **2023**, *4*, 2200404. [CrossRef]
10. Wang, N.; Song, S.; Wu, W.; Deng, Z.; Tang, C. Bridging laboratory electrocatalysts with industrially relevant alkaline water electrolyzers. *Adv. Energy Mater.* **2024**, *14*, 2303451. [CrossRef]
11. Han, C.; Lyu, Y.; Wang, S.; Liu, B.; Zhang, Y.; Weigand, J.J.; Du, H.; Lu, J. Highly utilized active sites on Pt@ Cu/C for ethanol electrocatalytic oxidation in alkali metal hydroxide solutions. *Adv. Funct. Mater.* **2023**, *33*, 2305436. [CrossRef]
12. Zhu, D.; Liu, J.; Zhao, Y.; Zheng, Y.; Qiao, S.Z. Engineering 2D metal–organic framework/MoS_2 interface for enhanced alkaline hydrogen evolution. *Small* **2019**, *15*, 1805511. [CrossRef] [PubMed]
13. González-Anota, D.E.; Castañeda-Morales, E.; Paredes-Carrera, S.P.; Manzo-Robledo, A. Modulating the HER-overpotential at the interface of nanostructured MoS_2 synthesized via hydrothermal route: An in-situ mass-spectroscopy approach. *Int. J. Hydrog. Energy* **2023**, *48*, 17852–17867. [CrossRef]
14. Kim, J.; Park, A.; Kim, J.; Kwak, S.J.; Lee, J.Y.; Lee, D.; Kim, S.; Choi, B.K.; Kim, S.; Kwag, J. Observation of H_2 evolution and electrolyte diffusion on MoS_2 monolayer by in situ liquid-phase transmission electron microscopy. *Adv. Mater.* **2022**, *34*, 2206066. [CrossRef]
15. Zhang, B.; Zhao, J.; Zhang, H.; Tian, J.; Cui, Y.; Zhu, W. Unveiling the Influences of In Situ Carbon Content on the Structure and Electrochemical Properties of MoS_2/C Composites. *Molecules* **2024**, *29*, 4513. [CrossRef]
16. Li, M.; Wang, X.; Du, H.; Dong, W.; Ye, S.; Liu, H.; Sun, H.; Huang, K.; Li, H.; Tang, Y. Oxophilic Tm-sites in MoS_2 trigger thermodynamic spontaneous water dissociation for enhanced hydrogen evolution. *Adv. Energy Mater.* **2024**, *14*, 2401716. [CrossRef]
17. Chanda, K.; Bairi, P.; Maiti, S.; Tripathi, A.; Thapa, R.; Ghosh, S.; Panigrahi, K.; Roy, D.; Sarkar, R.; Chattopadhyay, K.K. Crystallinity and interfacial Mo–N–C bond engineered MoS_2 embedded graphitic nitrogen doped carbon hollow sphere for enhanced HER activity. *Int. J. Hydrog. Energy* **2024**, *56*, 570–581. [CrossRef]
18. Hong, Z.; Hong, W.; Wang, B.; Cai, Q.; He, X.; Liu, W. Stable 1T–2H MoS_2 heterostructures for efficient electrocatalytic hydrogen evolution. *Chem. Eng. J.* **2023**, *460*, 141858. [CrossRef]
19. Guruprasad, K.; Maiyalagan, T.; Shanmugam, S. Phosphorus doped MoS_2 nanosheet promoted with nitrogen, sulfur dual doped reduced graphene oxide as an effective electrocatalyst for hydrogen evolution reaction. *ACS Appl. Energy Mater.* **2019**, *2*, 6184–6194. [CrossRef]
20. Huang, X.; Xu, H.; Cao, D.; Cheng, D. Interface construction of P-Substituted MoS_2 as efficient and robust electrocatalyst for alkaline hydrogen evolution reaction. *Nano Energy* **2020**, *78*, 105253. [CrossRef]
21. Peng, C.; Song, L.; Wang, L.; Yang, F.; Ding, J.; Huang, F.; Wang, Y. Effect of surface charge distribution of phosphorus-doped MoS_2 on hydrogen evolution reaction. *ACS Appl. Energy Mater.* **2021**, *4*, 4887–4896. [CrossRef]
22. Zhang, Y.; Yang, T.; Li, J.; Zhang, Q.; Li, B.; Gao, M. Construction of Ru, O Co-doping MoS_2 for hydrogen evolution reaction electrocatalyst and surface-enhanced Raman scattering substrate: High-performance, recyclable, and durability improvement. *Adv. Funct. Mater.* **2023**, *33*, 2210939. [CrossRef]
23. Guo, S.; Liu, Y.; Murphy, E.; Ly, A.; Xu, M.; Matanovic, I.; Pan, X.; Atanassov, P. Robust palladium hydride catalyst for electrocatalytic formate formation with high CO tolerance. *Appl. Catal. B Environ.* **2022**, *316*, 121659. [CrossRef]
24. Zhu, W.; Zhang, B.; Chen, T.; Shi, C.; Dong, X.; Tao, X. Structural regulation of 1T-MoS_2/Graphene composite materials for high-performance lithium-ion capacitors. *J. Energy Storage* **2024**, *102*, 114178. [CrossRef]
25. Fei, H.; Guo, T.; Xin, Y.; Wang, L.; Liu, R.; Wang, D.; Liu, F.; Wu, Z. Sulfur vacancy engineering of MoS_2 via phosphorus incorporation for improved electrocatalytic N2 reduction to NH_3. *Appl. Catal. B Environ.* **2022**, *300*, 120733. [CrossRef]
26. Xue, H.; Meng, A.; Chen, C.; Xue, H.; Li, Z.; Wang, C. Phosphorus-doped MoS_2 with sulfur vacancy defects for enhanced electrochemical water splitting. *Sci. China Mater.* **2022**, *65*, 712–720. [CrossRef]

27. Huang, J.; Chen, M.; Zhang, X.; Liu, W.; Liu, Y. P-doped 3D graphene network supporting uniformly vertical MoS_2 nanosheets for enhanced hydrogen evolution reaction. *Int. J. Hydrogen Energy* **2020**, *45*, 4043–4053. [CrossRef]
28. Li, S.; Luo, Z.; Wang, S.; Cheng, H. Atomic structure and HER performance of doped MoS_2: A mini-review. *Electrochem. Commun.* **2023**, *155*, 107563. [CrossRef]
29. Ma, G.; Zhou, Y.; Wang, Y.; Feng, Z.; Yang, J. N, P-codoped graphene supported few-layered MoS_2 as a long-life and high-rate anode materials for potassium-ion storage. *Nano Res.* **2021**, *14*, 3523–3530. [CrossRef]
30. Zhu, W.; Zhang, B.; Shi, C.; Cui, Y. 1T-MoS_2/C composite as an efficient electrocatalyst for hydrogen evolution reaction under alkaline condition. *J. Phys. Chem. Solids* **2024**, *185*, 111796. [CrossRef]
31. Zhan, W.; Zhang, X.; Yuan, Y.; Weng, Q.; Song, S.; Martínez-López, M.d.J.; Arauz-Lara, J.L.; Jia, F. Regulating chemisorption and electrosorption activity for efficient uptake of rare earth elements in low concentration on oxygen-doped molybdenum disulfide. *ACS Nano* **2024**, *18*, 7298–7310. [CrossRef] [PubMed]
32. Yang, Q.; Wang, Z.; Dong, L.; Zhao, W.; Jin, Y.; Fang, L.; Hu, B.; Dong, M. Activating MoS_2 with super-high nitrogen-doping concentration as efficient catalyst for hydrogen evolution reaction. *J. Phys. Chem. C* **2019**, *123*, 10917–10925. [CrossRef]
33. Sun, Z.; Lin, L.; Yuan, M.; Yao, H.; Deng, Y.; Huang, B.; Li, H.; Sun, G.; Zhu, J. Mott–Schottky heterostructure induce the interfacial electron redistribution of MoS_2 for boosting pH-universal hydrogen evolution with Pt-like activity. *Nano Energy* **2022**, *101*, 107563. [CrossRef]
34. Sun, W.; Li, P.; Liu, X.; Shi, J.; Sun, H.; Tao, Z.; Li, F.; Chen, J. Size-controlled MoS_2 nanodots supported on reduced graphene oxide for hydrogen evolution reaction and sodium-ion batteries. *Nano Res.* **2017**, *10*, 2210–2222. [CrossRef]
35. Fioravanti, F.; Martínez, S.; Delgado, S.; García, G.; Rodriguez, J.L.; Tejera, E.P.; Lacconi, G.I. Effect of MoS_2 in doped-reduced graphene oxide composites. Enhanced electrocatalysis for HER. *Electrochim. Acta* **2023**, *441*, 141781. [CrossRef]
36. Ruiz, K.H.; Liu, J.; Tu, R.; Li, M.; Zhang, S.; Garcia, J.R.V.; Mu, S.; Li, H.; Goto, T.; Zhang, L. Effect of microstructure on HER catalytic properties of MoS_2 vertically standing nanosheets. *J. Alloys Compd.* **2018**, *747*, 100–108. [CrossRef]
37. Chen, B.; Hu, P.; Yang, F.; Hua, X.; Yang, F.F.; Zhu, F.; Sun, R.; Hao, K.; Wang, K.; Yin, Z. In situ porousized MoS_2 nano islands enhance HER/OER bifunctional electrocatalysis. *Small* **2023**, *19*, 2207177. [CrossRef]
38. Joyner, J.; Oliveira, E.F.; Yamaguchi, H.; Kato, K.; Vinod, S.; Galvao, D.S.; Salpekar, D.; Roy, S.; Martinez, U.; Tiwary, C.S. Graphene supported MoS_2 structures with high defect density for an efficient HER electrocatalysts. *ACS Appl. Mater. Interfaces* **2020**, *12*, 12629–12638. [CrossRef]
39. Wu, L.; Xu, X.; Zhao, Y.; Zhang, K.; Sun, Y.; Wang, T.; Wang, Y.; Zhong, W.; Du, Y. Mn doped MoS_2/reduced graphene oxide hybrid for enhanced hydrogen evolution. *Appl. Surf. Sci.* **2017**, *425*, 470–477. [CrossRef]
40. Teich, J.; Dvir, R.; Henning, A.; Hamo, E.R.; Moody, M.J.; Cohen, H.; Marks, T.J.; Rosen, B.A.; Lauhon, L.J.; Ismach, A. Light and complex 3D MoS_2/graphene heterostructures as efficient catalysts for the hydrogen evolution reaction. *Nanoscale* **2020**, *12*, 2715–2725. [CrossRef]
41. Tahira, A.; Ibupoto, Z.H.; Mazzaro, R.; You, S.; Morandi, V.; Natile, M.M.; Vagin, M.; Vomiero, A. Advanced electrocatalysts for hydrogen evolution reaction based on core–shell MoS_2/TiO_2 nanostructures in acidic and alkaline media. *ACS Appl. Energy Mater* **2019**, *2*, 2053–2062. [CrossRef]
42. Zhang, Y.; Zhou, H.; Wang, H.; Zhang, Y.; Dionysiou, D.D. Synergistic effect of reduced graphene oxide and near-infrared light on MoS_2-mediated electrocatalytic hydrogen evolution. *Chem. Eng. J.* **2021**, *418*, 129343. [CrossRef]
43. Muthurasu, A.; Maruthapandian, V.; Kim, H.Y. Metal-organic framework derived Co_3O_4/MoS_2 heterostructure for efficient bifunctional electrocatalysts for oxygen evolution reaction and hydrogen evolution reaction. *Appl. Catal. B Environ.* **2019**, *248*, 202–210. [CrossRef]
44. Yu, X.; Zhao, G.; Gong, S.; Liu, C.; Wu, C.; Lyu, P.; Maurin, G.; Zhang, N. Design of MoS_2/graphene van der Waals heterostructure as highly efficient and stable electrocatalyst for hydrogen evolution in acidic and alkaline media. *ACS Appl. Mater. Interfaces* **2020**, *12*, 24777–24785. [CrossRef]
45. Narasimman, R.; Waldiya, M.; Jalaja, K.; Vemuri, S.K.; Mukhopadhyay, I.; Ray, A. Self-standing, hybrid three-dimensional-porous MoS_2/Ni_3S_2 foam electrocatalyst for hydrogen evolution reaction in alkaline medium. *Int. J. Hydrogen Energy* **2021**, *46*, 7759–7771. [CrossRef]

Disclaimer/Publisher's Note: The statements, opinions and data contained in all publications are solely those of the individual author(s) and contributor(s) and not of MDPI and/or the editor(s). MDPI and/or the editor(s) disclaim responsibility for any injury to people or property resulting from any ideas, methods, instructions or products referred to in the content.